

# Exploring Linear Attention Alternative for Single Image Super-Resolution\*

Rongchang Lu, Changyu Li, Donghang Li, Guojing Zhang, Jianqiang Huang, Xilai Li  
Qinghai University, Xining, China

**Abstract**—Deep learning-based single-image super-resolution (SISR) technology focuses on enhancing low-resolution (LR) images into high-resolution (HR) ones. Although significant progress has been made, challenges remain in computational complexity and quality, particularly in remote sensing image processing. To address these issues, we propose our Omni-Scale RWKV Super-Resolution (OmniRWKVSR) model which presents a novel approach that combines the Receptance Weighted Key Value (RWKV) architecture with feature extraction techniques such as Visual RWKV Spatial Mixing (VRSM) and Visual RWKV Channel Mixing (VRCM), aiming to overcome the limitations of existing methods and achieve superior SISR performance. This work has proved able to provide effective solutions for high-quality image reconstruction. Under the 4x Super-Resolution tasks, compared to the MambaIR model, we achieved an average improvement of 0.26% in PSNR and 0.16% in SSIM.

**Index Terms**—Deep Learning, Single Image Super-Resolution, Feature Extraction Techniques, Computational Complexity.

## I. INTRODUCTION

Single Image Super-Resolution (SISR) technology holds a significant position in the field of image processing, aiming to reconstruct LR images into HR images to meet the increasing demand for image clarity. SISR has broad application potential in various fields such as medical imaging [1], remote sensing [2], and video surveillance [3]. HR images not only provide more detailed visual information but also significantly enhance the accuracy of decision support, such as in medical diagnosis and environmental monitoring applications [4], [5].

Recent deep learning-based SISR methods have made significant strides in reconstructing LR images by training models on large numbers of LR/HR image pairs. Convolutional Neural Networks (CNNs) are commonly used for feature extraction, enabling detailed image recovery through multiple nonlinear transformations [6], [7]. However, challenges remain in applying SISR to remote sensing images, such as localized features, complex structures, scale differences, and noise [8]. To address these, several advanced models have been proposed. The SwinIR model leverages hierarchical feature representation and a shift-window-based self-attention mechanism for long-range dependency capture [9]. SwinFIR further enhances this by integrating a Fast Fourier Convolution (FFC) component for improved global information efficiency [10]. The MambaIR model, which applies the Mamba model for image restoration, combines convolution with channel attention mechanisms to improve representation [11], [12]. The Hybrid Attention Transformer (HAT) optimizes resource allocation and enhances feature extraction by selectively applying attention [13]. The

RWKV model [14], particularly its sixth generation (RWKV v6), improves training stability and convergence speed by integrating Recurrent Neural Networks (RNNs) and Transformer strengths while avoiding full attention mechanisms with linear complexity [15].

This study proposes a novel approach that combines the RWKV architecture with advanced feature extraction techniques and verified through ablation experiments, aiming to overcome the limitations of existing attention-based methods, such as the quadratic complexity. The main contributions of this study are as follows:

1) *Feed Forward Network*: ChannelMix is superior to traditional MLP in enhancing channel-wise feature mixing and improving information flow, thus outperforming MLP in feature extraction and image reconstruction quality.

2) *Omni-Quad Shift*: To capture long-range dependencies, we introduce a complementary mechanism: Omni-Quad Shift. It enables models to effectively capture multi-scale features and spatial transformations.

3) *Weighted Key Value (WKV) 2D Scanning*: Conventional linear models can only capture the one-dimensional information, which is also quoted "scanning". Despite the 2D scanning of Spate-Space model, the quality and performance still demand improving. To address this issue, the 2D scanning version of the WKV mechanism is proposed in this paper.

4) *Faster Training With SOTA Performance*: Our model reaches the highest score on popular datasets, such as Set14, BSD100 and so on with approximately 15% less training time compared to MambaIR.

## II. RELATED WORK

### A. Attention-based Super Resolution

In recent years, attention mechanisms have significantly advanced SISR by enabling models to effectively capture long-range dependencies and focus on critical image regions. Notably, the Swin Transformer-based model, SwinIR [9], has demonstrated exceptional performance across various image restoration tasks, including super-resolution, denoising, and JPEG artifact reduction [16], [17].

Despite the significant advancements brought by attention mechanisms in SISR [9], [18], a notable limitation persists: the computational complexity of self-attention operations scales quadratically with the input size. This quadratic complexity arises because the attention mechanism computes pairwise interactions between all elements in the input sequence, leading

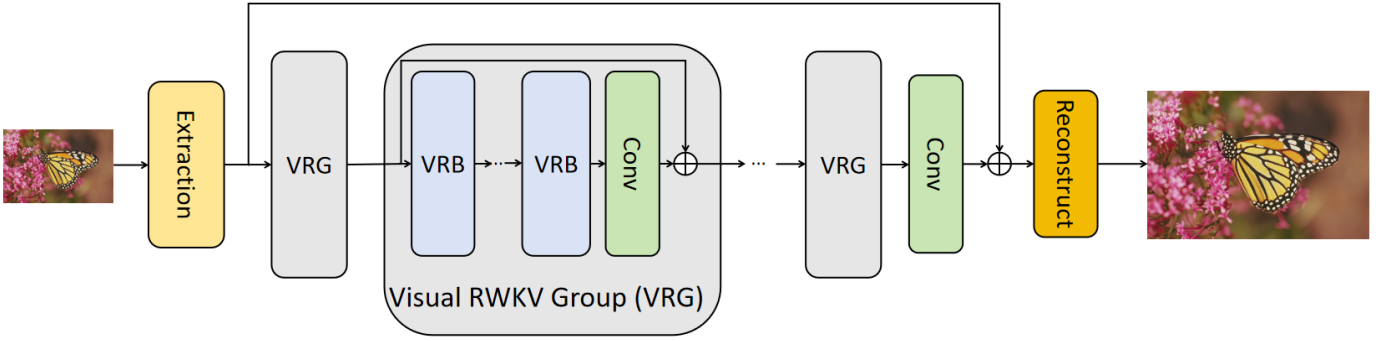


Fig. 1. The architecture of OmniRWKVSr.

to substantial computational and memory demands, especially for HR images.

### B. State Space Model (SSM)

To address the computational challenges of attention-based SISR, several models [9], [10] have integrated innovative mechanisms to improve efficiency. The MambaIR model [11] introduces a Selective State Space 2D (SS2D) mechanism [19], [20], which employs SSM with selective scanning strategies to capture long-range dependencies while maintaining linear computational complexity relative to the input size. This design effectively reduces the computational burden of traditional quadratic attention mechanisms, making MambaIR scalable and efficient for HR image restoration tasks. The SS2D mechanism allows MambaIR to model intricate image details without incurring the prohibitive costs typical of self-attention methods, thus balancing performance and efficiency for large-scale image processing.

### C. RWKV Structure

Despite the advancements introduced by MambaIR [11] and the SS2D [12] mechanism, challenges remain in terms of prolonged training times, unstable performance metrics, rapid convergence, and suboptimal feature extraction capabilities. The RWKV v6 [14] offers solutions to these issues by integrating the strengths of RNNs and Transformers while eliminating the reliance on attention mechanisms. One of the key improvements in RWKV v6 is its improved training stability and convergence speed. By employing careful initialization strategies and optimized training protocols, RWKV v6 mitigates issues related to training instability and premature convergence, leading to more robust and reliable performance across various tasks. Additionally, RWKV's linear computational complexity with respect to input sequence length addresses the inefficiencies associated with quadratic complexity in traditional attention mechanisms. Hence, in this paper, we propose this innovative approach that integrates the strengths of the RWKV architecture with advanced feature extraction techniques to enhance SISR tasks.

## III. METHOD

This section first details the overall pipeline of our proposed OmniRWKVSr model and then explains the basic block of the network: Visual RWKV Residual Group (VRG).

### A. OmniRWKVSr Model

The overall structure of Omni-Scale RWKV model is shown in Fig. 1. We denote the LR input image as  $\mathbf{I}_{LR} \in \mathbb{R}^{B \times C \times H \times W}$ , and the HR target image as  $\mathbf{I}_{HR} \in \mathbb{R}^{B \times C \times H \times W}$ .

Initially, we use a  $3 \times 3$  CNN layer, worked as the shallow feature extractor (Extraction), to extract low-level features from the LR input image.

Secondly, we use multiple VRGs to extract high-level features from  $\mathbf{F}_{\text{embd}}^1$ , denoted as  $\mathbf{F}_{\text{feat}}$ :

$$\mathbf{F}_{\text{embd}}^n = f_{VRG}^n(f_{VRG}^{n-1}(\dots f_{VRG}^1(\mathbf{F}_{\text{embd}}^1))), \quad (1)$$

where  $f_{VRG}^n$  is a VRG,  $\mathbf{F}_{\text{embd}}^0$  is the output of the shallow feature extractor, and  $f_{VRG}^{n-1}(\dots f_{VRG}^1(\mathbf{F}_{\text{embd}}^0))$  is the output of the previous VRG.

Thirdly, we use a  $3 \times 3$  CNN layer and a one-step upsampling operation (Reconstruct) to upsample  $\mathbf{F}_{\text{embd}}$  to the HR resolution, denoted as  $\mathbf{F}_{HR}$ :

$$\mathbf{F}_{HR} = \text{upsample}(\text{conv}_{\text{feat}}(\mathbf{F}_{\text{embd}}^n)), \quad (2)$$

where  $\text{conv}_{\text{feat}}$  is a  $3 \times 3$  CNN layer,  $\mathbf{F}_{\text{embd}}^n$  is the output of the n-th VRG, and  $\text{upsample}$  is a one-step upsampling operation.

Finally, we add the mean and variance back to  $\mathbf{F}_{HR}$  and obtain the high-quality reconstructed image, denoted as  $\mathbf{I}_{HR}$ :

$$\mathbf{I}_{HR} = \mu_{LR} + \sigma_{LR} \odot \mathbf{F}_{HR}, \quad (3)$$

where  $\odot$  is the element-wise multiplication operator,  $\mu_{LR}$  and  $\sigma_{LR}$  are the mean and variance of the LR input image, respectively.

### B. Visual RWKV Group

A VRG is a collection of residual blocks that integrates the VRSM and VRCM as its core components. The VRSM facilitates the blending of feature maps across different resolutions, while the VRCM confines these features to specific

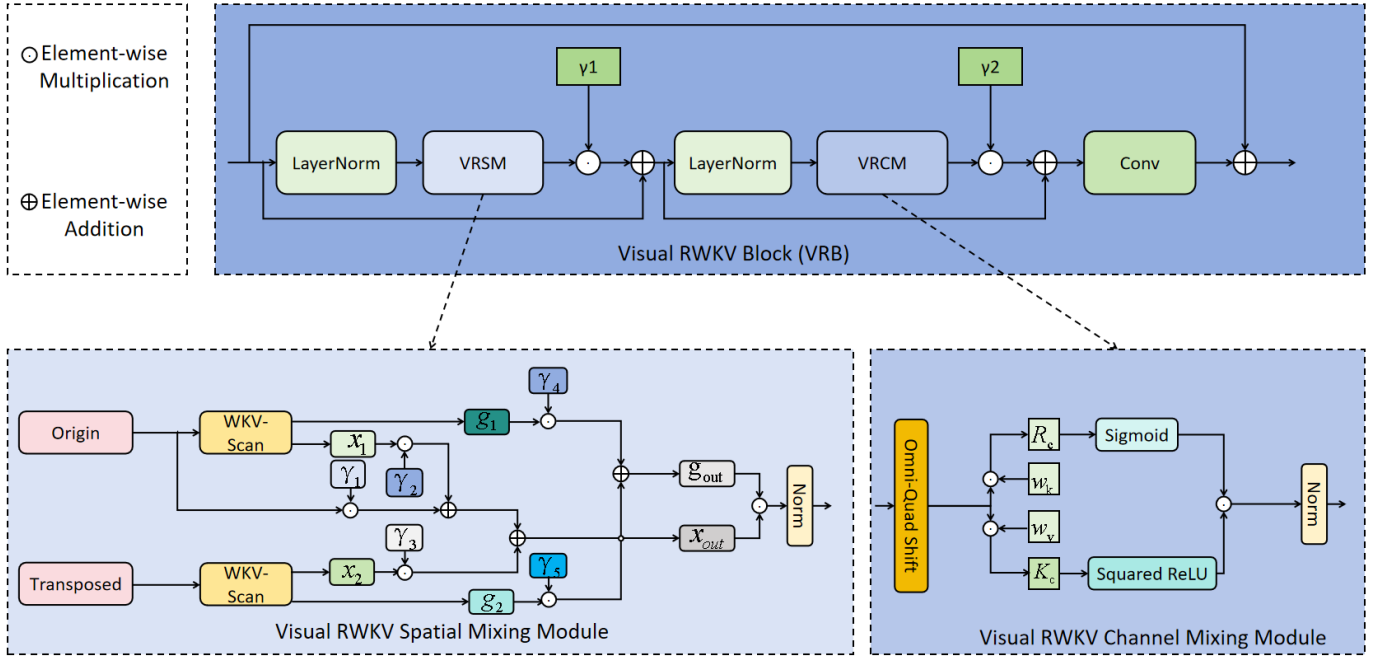


Fig. 2. The architecture of VRB, VRSM and VRCM.

channels. A VRG is composed of multiple Visual RWKV Residual Blocks (VRBs), and the overall structure of the VRB is shown in Fig. 2.

The VRG receives input from either the output of the previous VRG or the shallow feature extractor, and its output is directed to the subsequent VRG or the process for high-quality reconstruction. Features entering VRSM are initially subjected to a shift operation using Omni-Quad Shift, yielding a set of shifted feature maps that encapsulate the features of neighboring pixels. These maps are then integrated through a channel-wise linear attention mechanism within the Spatial Mixing operation, which selects significant channels and conducts 2D scan operations to reassemble the feature maps. The outcome is fed back into the input feature map through a residual connection. Following this, the output is directed to VRCM, which confines the feature maps to specific channels, with its output also reintegrated via a residual connection. The VRCM output is then passed through a  $3 \times 3$  convolutional layer, added back to the input feature map through a residual connection, and advanced to the next residual block or the high-quality reconstruction phase.

### C. WKV2DScan

The WKV2DScan module is a two-stage process that operates on an input tensor to yield feature maps and attention weights. The visual illustration of WKV2DScan is shown as Fig. 3, where the scanning operation is performed horizontally and vertically to obtain the features in both directions. In each stage of WKV2DScan, a WKV-Scan operation is performed. WKV-Scan initiates with a shift operation to gather contextual data, defining the shifted tensor as  $\mathbf{x}_{ssh}$ :

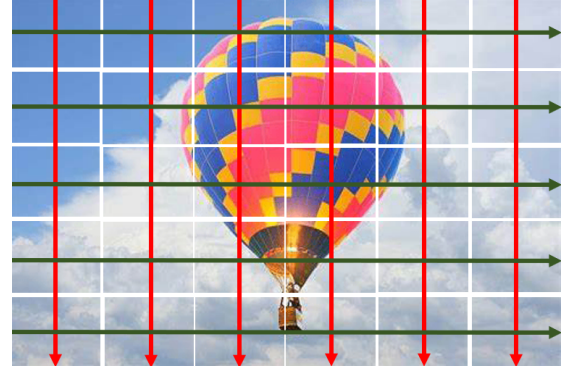


Fig. 3. Visual illustration for WKV2DScan.

$$\mathbf{x}_{ssh}^n = f_{\text{Omni-Quad Shift}}(\mathbf{x}_{in}^n), \quad (4)$$

which is followed by a weighted sum calculation, combining the shifted tensor with the original to produce  $\mathbf{x}_{ss}$ .

$$\mathbf{x}_{ss}^n = \mathbf{x}_{ssh}^n \odot \mathbf{tma}_x + \mathbf{tma}_{xb}, \quad (5)$$

where  $\mathbf{tma}_x$  is the time-dependent moving average of the input tensor, and  $\mathbf{tma}_{xb}$  is the bias term.

Subsequently, the module calculates key parameters for the scan operation. These include learnable weights and time-dependent moving averages, which are determined by the formulas:

$$\begin{pmatrix} r_s^n \\ k_s^n \\ v_s^n \\ g_s^n \\ ww_s^n \end{pmatrix} = \begin{pmatrix} w_r \\ w_k \\ w_v \\ w_g \\ w_{ww} \end{pmatrix} \left( \mathbf{x}_{in}^n + \mathbf{x}_{ssh}^n \left( \begin{pmatrix} tma_r \\ tma_k \\ tma_v \\ tma_g \\ tma_r \end{pmatrix} \oplus \mathbf{x}_{ss}^n \right) \right), \quad (6)$$

where  $w_r, w_k, w_v, w_g, w_{ww}$  are the learnable weights that is shared during two scans, while the  $tma_r, tma_k, tma_v, tma_g$ , are ones that exist on their respective scans, so that not only are they dependent, but also can be learned from either scan during training.

The scanned feature map is then derived using the WKV6 module, with the formula:

$$\mathbf{x}_{out}^n = \text{WKV6}(H, r, k, v, w, u), \quad (7)$$

where  $H$  represents the head size.

The first WKV-Scan operation is applied to the input feature map  $F_{\text{embd}}^n$ , yielding the first set of scanned feature maps and attention weights  $\mathbf{x}_{o1}^n, \mathbf{g}_{o1}^n$ . For the second operation, the transposed input feature map  $F_{\text{embd}}^{nT}$  is used to obtain the second set  $\mathbf{x}_{o2}^n, \mathbf{g}_{o2}^n$ .

Finally, the WKV2DScan module outputs a tuple of the scanned feature maps and attention weights, computed as:

$$\mathbf{x}_{out}^n = F_{\text{embd}}^n \odot \gamma_{s1}^n + \mathbf{x}_{o1}^n \odot \gamma_{s2}^n + \mathbf{x}_{o2}^n \odot \gamma_{s3}^n, \quad (8)$$

$$\mathbf{g}_{out}^n = \text{Sigmoid}(\mathbf{g}_{o1}^n \odot \gamma_{s4}^n + \mathbf{g}_{o2}^n \odot \gamma_{s5}^n), \quad (9)$$

$$\mathbf{y}_{out} = \mathbf{x}_{out}^n \odot \mathbf{g}_{out}^n, \quad (10)$$

where  $\gamma_{s1}^n, \gamma_{s2}^n, \gamma_{s3}^n, \gamma_{s4}^n, \gamma_{s5}^n$  are learnable weights, and  $\mathbf{y}_{out}$  is the output of VRSM.

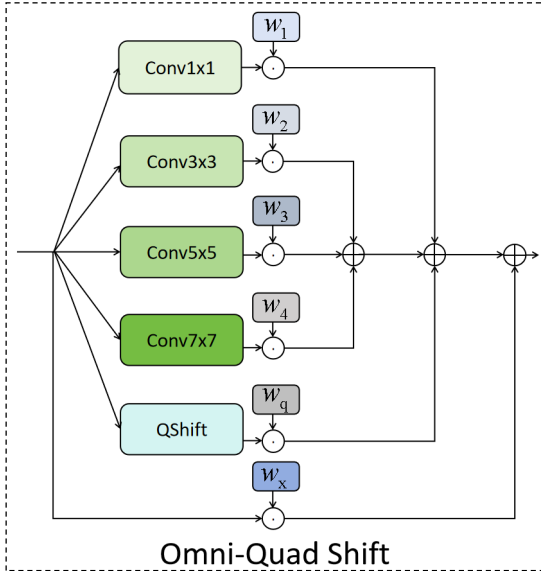


Fig. 4. The architecture of Omni-Quad Shift.

#### D. Omni-Quad Shift

Our Omni-Quad Shift leverages multi-scale convolutional kernels ( $1 \times 1$ ,  $3 \times 3$ ,  $5 \times 5$ , and  $7 \times 7$ ) to aggregate information at different receptive field sizes. Each convolutional kernel is depthwise and dilated, capturing both local and global features. The outputs are combined using learnable weights to produce a unified representation. Of these convolutions,  $\text{Conv}_{1 \times 1}(\mathbf{X})$  captures point-wise features,  $\text{Conv}_{3 \times 3}(\mathbf{X})$  extracts local spatial details,  $\text{Conv}_{5 \times 5}(\mathbf{X})$  enhances mid-range dependencies and  $\text{Conv}_{7 \times 7}(\mathbf{X})$  expands the receptive field for global context. Also, learnable weights  $w_x, w_1, w_2, w_3, w_4, w_q$  modulate the contribution of each convolution and Quad-directional Shift (QShift):

$$\mathbf{Y} = \begin{pmatrix} w_x \\ w_1 \\ w_2 \\ w_3 \\ w_4 \\ w_q \end{pmatrix}^T \begin{pmatrix} \mathbf{X} \\ \text{Conv}_{1 \times 1}(\mathbf{X}) \\ \text{Conv}_{3 \times 3}(\mathbf{X}) \\ \text{Conv}_{5 \times 5}(\mathbf{X}) \\ \text{Conv}_{7 \times 7}(\mathbf{X}) \\ \text{QShift}(\mathbf{X}) \end{pmatrix}, \quad (11)$$

After obtaining the output tensor  $\mathbf{Y}$ , we rearrange the output back into the original spatial format.

## IV. EXPERIMENT

### A. Dataset and implementation details

The training and validation set consisted of 2650 images from Flickr2K [21], 800 images from DIV2K [22], and 2800 images from RSSCN7 [23] total, of which the training set occupies 95%. In the Flickr2K and DIV2K dataset (DF2K), the image resolution is  $2048 \times 2048$  and  $2048 \times 1080$  pixels. In the RSSCN7 dataset, the image resolution is  $400 \times 400$  pixels. The resolution of LR in the training set is fixed to  $48 \times 48$ , while that of HR is  $96 \times 96$  at a 2x scale factor and  $192 \times 192$  at 4x one. Our experiments were carried out to ensure that all trained hyperparameters and the number of parameters were approximately the same. Our models were evaluated on widely used benchmark datasets: Set5 [24], Set14 [25], BSD100 [26], Urban100 [27] and Manga109 [28]. We also performed tests on our own Gangcha MouseHole (GMH) remote sensing dataset, the validation set of the DF2K dataset, and the public RSSCN7 remote sensing dataset.

The GMH dataset is captured by a DJI Mavic 3E drone in Qinghai Province, China, which includes 325 images of mouse holes in the middle reaches at an altitude of 30 meters, 222 images of mouse holes in the upper reaches at an altitude of 40 meters, and 60 images of mouse holes in the middle and upper reaches at an altitude of 80 meters over the grasslands of Gangcha County. In total, there are 607 images, each with a resolution of  $5280 \times 3956$  pixels split into  $72 \times 72$  LR pieces to perform SR tasks.

RSSCN7 [23] is a remote sensing image dataset for scene classification, featuring 2800 high-resolution RGB images at  $400 \times 400$  pixels. It includes seven classes: grassland, forest, farmland, industrial/commercial, river/lake, residential, and parking lots, with 400 images each.

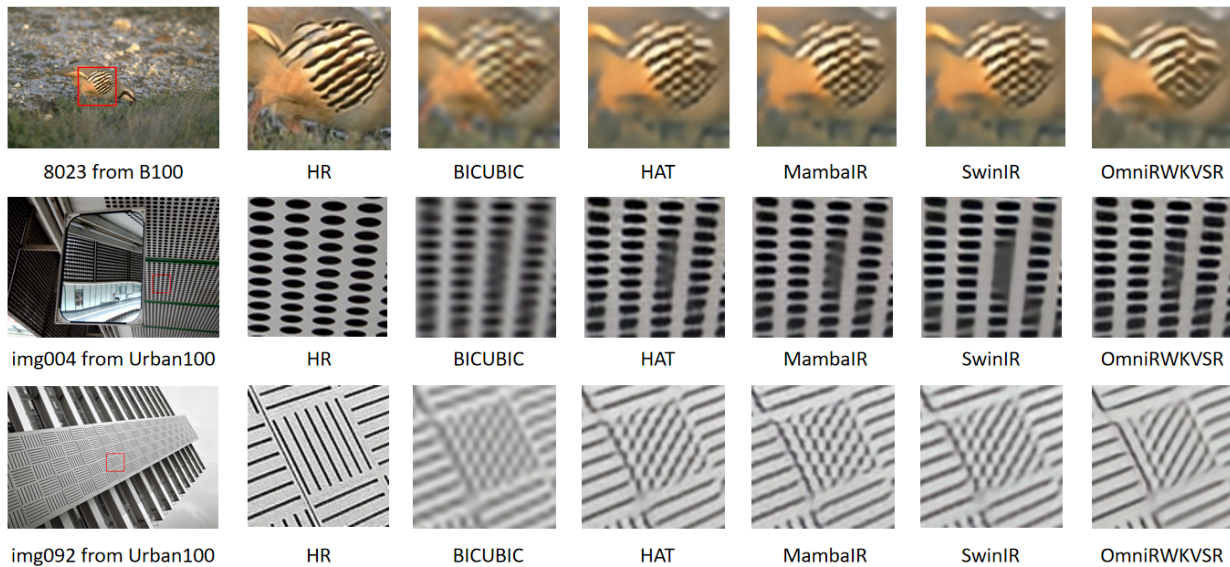


Fig. 5. Visual results on benchmark datasets for  $\times 4$  super-resolution.

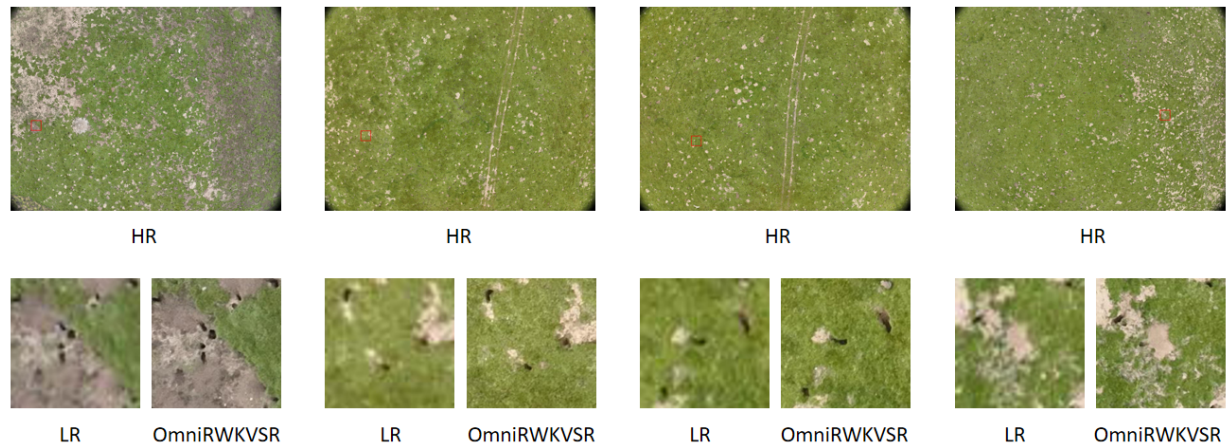


Fig. 6. Visual results on Gangcha MouseHole dataset.

Our model is trained on RGB channels and augmented data with random rotations, sizes and flipping. The PSNR [29] and SSIM [30] on the Y channel in the YCbCr space is calculated as quantitative measurements. Our implementation of OmniRWKVSr contains 96 channels and 16 VRG blocks. The minibatch size is set to 16, using Adam optimizer for optimization. In the first stage, a pre-training of 20000 iterations is performed using  $\mathcal{L}_1$  Loss function, and the learning rate is set to  $1e-4$ . We use none of learning rate scheduler so as to ensure our model can keep its performance without any tricks for training.

### B. Qualitative evaluations

Fig. 5 presents a qualitative comparison of the proposed method at a 4x scale factor on the Set14 and Urban100 datasets. The figure displays the visual effects of HR, BICUBIC, HAT [13], MambaIR [11], SwinIR [9], and OmniRWKVSr (our work) on the specified images.

Taking “img092” as an example, both MambaIR and SwinIR have issues in restoring stripe textures, where the stripes appear blurry and interlaced. Our method also faces challenges in achieving high-quality super-resolution reconstruction due to the significant difference between the test set and the training set. However, OmniRWKVSr performs relatively better in this regard. It can more accurately recover the characteristics of stripes, making them clearer and more realistic compared to other methods. While ensuring lightweight complexity, OmniRWKVSr is able to effectively achieve better super-resolution reconstruction results under the given circumstances.

### C. Quantitative evaluations

To comprehensively evaluate the effectiveness of OmniRWKVSr in terms of image super-resolution reconstruction quality, we conducted a detailed comparison with several SOTA super-resolution models, including SwinIR [9], Swin-

TABLE I  
COMPARISON OF OMNI<sub>RWKVSR</sub> AND SOTA SUPER-RESOLUTION MODELS ACROSS DIFFERENT DATASETS. BOLD DATA INDICATE THE BEST METHOD.

Scale	Models	DF2K+RSSCN7 PSNR/SSIM $\uparrow$	Set5 PSNR/SSIM $\uparrow$	Set14 PSNR/SSIM $\uparrow$	BSD100 PSNR/SSIM $\uparrow$	Urban100 PSNR/SSIM $\uparrow$	Manga109 PSNR/SSIM $\uparrow$	Gangcha MouseHole PSNR/SSIM $\uparrow$
x2	<b>OmniRWKVSR(ours)</b>	<b>31.86/0.8558</b>	<b>35.36/0.9318</b>	<b>31.74/0.8737</b>	<b>30.63/0.8517</b>	<b>29.43/0.8860</b>	<b>35.42/0.9513</b>	<b>33.02/0.8281</b>
	MambaIR [11]	31.86/0.8555	35.34/0.9290	31.75/0.8737	30.60/0.8498	29.29/0.8801	35.32/0.9506	33.01/0.8279
	SwinIR [9]	31.79/0.8536	35.34/0.9317	31.75/0.8749	30.60/0.8496	29.29/0.8775	35.32/0.9512	32.99/0.8264
	SwinFIR [10]	31.78/0.8539	35.35/0.9318	31.76/0.8752	30.62/0.8502	29.31/0.8780	35.30/0.9509	32.98/0.8259
	HAT [13]	31.77/0.8547	<b>35.36/0.9319</b>	31.77/0.8755	30.63/0.8516	29.38/0.8797	35.32/0.9514	33.01/0.8280
	MambaIRv2 [31]	31.86/0.8554	35.28/0.9310	31.69/0.8765	<b>30.64/0.8517</b>	29.42/0.8837	35.42/0.9522	33.00/0.8281
x4	<b>OmniRWKVSR(ours)</b>	<b>28.07/0.7192</b>	<b>30.14/0.8458</b>	<b>27.34/0.7264</b>	<b>26.66/0.6809</b>	<b>24.58/0.7160</b>	<b>27.89/0.8533</b>	<b>29.17/0.6358</b>
	MambaIR [11]	28.04/0.7188	30.01/0.8445	27.29/0.7255	26.63/0.6801	24.50/0.7141	27.73/0.8501	29.15/0.6355
	SwinIR [9]	27.98/0.7168	29.99/0.8439	27.23/0.7257	26.60/0.6804	24.39/0.7091	27.43/0.8435	29.14/0.6354
	SwinFIR [10]	27.98/0.7170	29.99/0.8442	27.23/0.7260	26.60/0.6803	24.41/0.7099	27.46/0.8442	29.13/0.6355
	HAT [13]	28.01/0.7179	30.08/0.8459	27.29/0.7276	26.63/0.6814	24.48/0.7131	27.61/0.8467	29.15/0.6357
	MambaIRv2 [31]	28.04/0.7192	30.11/0.8468	27.32/0.7285	26.67/0.6827	24.57/0.7179	27.80/0.8517	29.16/0.6358

TABLE II  
TRAINING AND INFERENCE TIME AND OPERATIONS COMPARISON OF DIFFERENT MODELS

Model	Training	Inference	Parameters[M]	FLOPs[G]
<b>OmniRWKVSR (ours)</b>	3h 47min 58sec	19min 34sec	2.96	112.46
MambaIR [11]	4h 32min 12sec	21min 12sec	2.87	121.28
MambaIRv2 [31]	5h 9min 9sec	22min 55sec	3.12	121.26
SwinIR [9]	5h 18min 45sec	25min 23sec	2.78	154.95

FIR [10], MambaIR [11], and its improved version MambaIRv2 [31]. All comparisons were made at scale factors of  $\times 4$  and  $\times 2$ . OmniRWKVSR significantly enhances its representation capabilities by integrating local information processing convolutions and channel attention mechanisms. We compare OmniRWKVSR with other models on training and inference time.

According to the data in TABLE I, at a scale factor of  $\times 4$ , OmniRWKVSR demonstrates excellent performance across several key performance metrics. On the DF2K+RSSCN7 validation dataset, OmniRWKVSR achieved a PSNR of 28.0720 dB and an SSIM of 0.7192, placing it at the forefront among all compared models. Particularly on the Set5 dataset, OmniRWKVSR’s PSNR and SSIM reached 30.1390 dB and 0.8458, respectively, indicating a clear advantage in preserving image details and structure. On the Urban100 dataset, OmniRWKVSR’s PSNR and SSIM were 24.5824 dB and 0.7160, slightly lower than MambaIRv2, but still showing strong competitiveness. On the Manga109 dataset, OmniRWKVSR’s PSNR and SSIM were 27.8930 dB and 0.8533, respectively, which not only surpasses all other models, especially in terms of structural similarity, but also sets a new benchmark for super-resolution in manga-style images, where preserving the intricate line details and color gradients is crucial.

As for training and inference speed, TABLE II shows the result. All training and inference processes are conducted on an NVIDIA A800 40G GPU. Inference involves performing super-resolution on all images across the datasets listed in Table I. From the perspective of time complexity and compu-

tational efficiency, our model, OmniRWKVSR, demonstrates superior performance due to its highly optimized CUDA kernels and linear computational complexity. In contrast, models like SwinIR [9] utilize Window Attention to improve computational efficiency; however, this mechanism still operates with quadratic complexity, leading to slower training and inference times. While MambaIR and its derivatives, such as SS2D and Attentive SSM [31], also exhibit linear complexity, their computational efficiency does not match that of OmniRWKVSR. This disparity can be attributed to the less optimized CUDA operations in these models, which result in longer processing times compared to our approach. The combination of efficient CUDA operations and linear complexity allows OmniRWKVSR to achieve faster processing while maintaining high performance.

We have also included the Floating Point Operations (FLOPs) in our comparison, which represent the total number of floating-point operations that a network performs when processing a  $217 \times 207$  pixel image. A lower FLOP count signifies a more computationally efficient model. Compared to other models, OmniRWKVSR achieves the lowest FLOPs, which indicates that our model effectively reduces computational complexity. The computations are performed using torch-operation-counter [32].

#### D. Ablation study

In the field of SISR, understanding the impact of individual components within a model is crucial for optimizing performance. To this end, we conducted a systematic ablation study on our proposed OmniRWKVSR, focusing on three key components: the feed forward network, the shift mechanism, and the WKV2D scan module.

1) *Feed Forward Network*: The feed forward network is a fundamental element in our model, and we compared the traditional Multi-Layer Perceptron (MLP) with our proposed ChannelMix. While the MLP is a commonly used architecture that transforms features through multiple fully connected layers, it may not effectively capture complex inter-channel

TABLE III  
ABLATION STUDY RESULTS

Component	Method	PSNR	SSIM
Feed Forward Network	MLP	28.0689	0.7188
	<b>ChannelMix</b>	<b>28.0720</b>	<b>0.7192</b>
Shift Mechanism	OmniShift [33]	30.1034	0.8453
	QShift [34]	30.0965	0.8411
	<b>Quad-Omni Shift</b>	<b>30.1390</b>	<b>0.8458</b>
WKV2D Scan	WKV Scan [11]	30.1149	0.8449
	<b>WKV2D Scan</b>	<b>30.1390</b>	<b>0.8458</b>

interactions. In contrast, ChannelMix is designed to enhance channel-wise feature mixing, improving information flow. Our results (TABLE III) indicated that ChannelMix outperformed the MLP in terms of both PSNR (28.0720) and SSIM (0.7192), compared to MLP (PSNR 28.0689, SSIM 0.7188) under validation. This suggests that ChannelMix is superior in feature extraction and image reconstruction quality.

2) *Shift Mechanism*: The shift mechanism is another critical component of our model, and we evaluated three different mechanisms: OmniShift [33], QShift [34], and Quad-Omni Shift. OmniShift captures local spatial dependencies through uniform shifting but has limitations in capturing long-range dependencies. QShift enhances the ability to capture both local and global spatial dependencies by applying different shifts to different parts of the input features. Quad-Omni Shift combines the strengths of both, utilizing a multi-scale shifting strategy that effectively manages various spatial dependencies. In our evaluation using the Set14 dataset, Quad-Omni Shift achieved a PSNR of 30.1390 and an SSIM of 0.8458, outperforming both OmniShift (PSNR 30.1034, SSIM 0.8453) and QShift (PSNR 30.0965, SSIM 0.8411) under test on Set14 dataset, demonstrating its effectiveness in capturing multi-scale features and spatial transformations.

3) *WKV2D Scan*: Lastly, we compared the original WKV Scan with the newly proposed WKV2D Scan. The WKV Scan employs a 1D scanning approach, which may not fully capture the spatial dependencies within the image. In contrast, WKV2D Scan extends this to a 2D scanning mechanism, allowing for comprehensive capture of both horizontal and vertical spatial dependencies. In our experiments on the Set14 dataset, WKV2D Scan significantly outperformed WKV Scan, achieving a PSNR of 30.1390 and an SSIM of 0.8458, compared to WKV Scan (PSNR 30.1149, SSIM 0.8449) under test on Set14 dataset. This indicates that WKV2D Scan has a clear advantage in processing input features and generating accurate attention weights.

## V. CONCLUSION

This research contributes to the advancement of image restoration technology, providing effective solutions for applications requiring high-quality image reconstruction and demonstrating superior performance in this task from LR inputs. OmniRWKVSr effectively overcomes the limitations

of existing attention-based methods, such as high computational complexity and suboptimal feature extraction capabilities, by leveraging the linear computational complexity and training efficiency of the RWKV model. Through extensive experiments, we show that our model achieved state-of-the-art results in terms of PSNR and SSIM metrics on various benchmark datasets, including Set5, Set14, BSD100, Urban100, and Manga109. The qualitative results further validate the model’s ability to produce clear and noise-free super-resolution images. The ablation study highlights the importance of each component in enhancing the overall performance of the model.

Although our model shows superior performance in terms of PSNR and SSIM, there are still issues such as texture errors and lack of clarity in the visualized results. Moreover, the performance on the GMH dataset is not satisfactory. Future work will focus on addressing these problems.

## REFERENCES

- [1] F. Lin, J. D. Rojas, and P. A. Dayton, “Super resolution contrast ultrasound imaging: Analysis of imaging resolution and application to imaging tumor angiogenesis,” in *2016 IEEE International Ultrasonics Symposium (IUS)*. IEEE, 2016, pp. 1–4.
- [2] M. R. Khosravi and P. Tavallali, “Real-time statistical image and video processing for remote sensing and surveillance applications,” *Journal of Real-Time Image Processing*, vol. 18, pp. 1435–1439, 2021.
- [3] F. Rezaei and M. Yazdi, “Real-time crowd behavior recognition in surveillance videos based on deep learning methods,” *Journal of Real-Time Image Processing*, vol. 18, no. 5, pp. 1669–1679, 2021.
- [4] W. Yang, X. Zhang, Y. Tian, W. Wang, J.-H. Xue, and Q. Liao, “Deep learning for single image super-resolution: A brief review,” *IEEE Transactions on Multimedia*, vol. 21, no. 12, pp. 3106–3121, 2019.
- [5] J. Li, Z. Pei, and T. Zeng, “From beginner to master: A survey for deep learning-based single-image super-resolution,” *arXiv e-prints*, pp. arXiv–2109, 2021, online.
- [6] J. Su, B. Xu, and H. Yin, “A survey of deep learning approaches to image restoration,” *Neurocomputing*, vol. 487, pp. 46–65, 2022.
- [7] A. Wali, A. Naseer, M. Tamoor, and S. Gilani, “Recent progress in digital image restoration techniques: a review,” *Digital Signal Processing*, p. 104187, 2023.
- [8] D. Dai, Y. Wang, Y. Chen, and L. Van Gool, “Is image super-resolution helpful for other vision tasks?” in *2016 IEEE Winter Conference on Applications of Computer Vision (WACV)*. IEEE, 2016, pp. 1–9.
- [9] J. Liang, J. Cao, G. Sun, K. Zhang, L. Van Gool, and R. Timofte, “Swinir: Image restoration using swin transformer,” in *Proceedings of the IEEE/CVF International Conference on Computer Vision*, 2021, pp. 1833–1844.
- [10] D. Zhang, F. Huang, S. Liu, X. Wang, and Z. Jin, “Swinfir: Revisiting the swinir with fast fourier convolution and improved training for image super-resolution,” *arXiv preprint arXiv:2208.11247*, 2022, online.
- [11] H. Guo, J. Li, T. Dai, Z. Ouyang, X. Ren, and S. Xia, “Mambair: A simple baseline for image restoration with state-space model,” in *European Conference on Computer Vision*. Springer, 2025, pp. 222–241.
- [12] L. Zhu, B. Liao, Q. Zhang, X. Wang, W. Liu, and X. Wang, “Vision mamba: Efficient visual representation learning with bidirectional state space model,” *arXiv preprint arXiv:2401.09417*, 2024, online.
- [13] X. Chen, X. Wang, J. Zhou, Y. Qiao, and C. Dong, “Activating more pixels in image super-resolution transformer,” in *Proceedings of the IEEE/CVF conference on computer vision and pattern recognition*, 2023, pp. 22 367–22 377.
- [14] B. Peng, E. Alcaide, Q. Anthony, A. Albalak, S. Arcadinho, S. Biderman *et al.*, “Rwkv: Reinventing rns for the transformer era,” *arXiv preprint arXiv:2305.13048*, 2023, online.
- [15] B. Peng, D. Goldstein, Q. Anthony, A. Albalak, E. Alcaide, S. Biderman *et al.*, “Eagle and finch: Rwkv with matrix-valued states and dynamic recurrence,” *arXiv preprint arXiv:2404.05892*, 2024, online.
- [16] A. E. Ilesanmi and T. O. Ilesanmi, “Methods for image denoising using convolutional neural network: a review,” *Complex & Intelligent Systems*, vol. 7, no. 5, pp. 2179–2198, 2021.

- [17] J. Hu, G. Luo, B. Wang, W. Wu, J. Yang, and J. Guo, "Residual network for image compression artifact reduction," *International Journal of Pattern Recognition and Artificial Intelligence*, vol. 38, no. 02, p. 2454001, 2024.
- [18] A. Dosovitskiy, "An image is worth 16x16 words: Transformers for image recognition at scale," *arXiv preprint arXiv:2010.11929*, 2020, online.
- [19] A. Gu, K. Goel, and C. Ré, "Efficiently modeling long sequences with structured state spaces," *arXiv preprint arXiv:2111.00396*, 2021, online.
- [20] A. Gu and T. Dao, "Mamba: Linear-time sequence modeling with selective state spaces," *arXiv preprint arXiv:2312.00752*, 2023, online.
- [21] Y. Li, K. Zhang, J. Liang, J. Cao, C. Liu, R. Gong *et al.*, "Lsdir: A large scale dataset for image restoration," in *Proceedings of the IEEE/CVF Conference on Computer Vision and Pattern Recognition*, 2023, pp. 1775–1787.
- [22] E. Agustsson and R. Timofte, "Ntire 2017 challenge on single image super-resolution: Dataset and study," in *Proceedings of the IEEE conference on computer vision and pattern recognition workshops*, 2017, pp. 126–135.
- [23] Y. Gao, J. Shi, J. Li, and R. Wang, "Remote sensing scene classification based on high-order graph convolutional network," *European Journal of Remote Sensing*, vol. 54, no. sup1, pp. 141–155, 2021.
- [24] M. Bevilacqua, A. Roumy, C. Guillemot, and M. L. Alberi-Morel, "Low-complexity single-image super-resolution based on nonnegative neighbor embedding," 2012.
- [25] R. Zeyde, M. Elad, and M. Protter, "On single image scale-up using sparse-representations," in *Curves and Surfaces: 7th International Conference, Avignon, France, June 24-30, 2010, Revised Selected Papers 7*. Springer, 2012, pp. 711–730.
- [26] D. Martin, C. Fowlkes, D. Tal, and J. Malik, "A database of human segmented natural images and its application to evaluating segmentation algorithms and measuring ecological statistics," in *Proceedings eighth IEEE international conference on computer vision. ICCV 2001*, vol. 2. IEEE, 2001, pp. 416–423.
- [27] J.-B. Huang, A. Singh, and N. Ahuja, "Single image super-resolution from transformed self-exemplars," in *Proceedings of the IEEE conference on computer vision and pattern recognition*, 2015, pp. 5197–5206.
- [28] Y. Matsui, K. Ito, Y. Aramaki, A. Fujimoto, T. Ogawa, T. Yamasaki *et al.*, "Sketch-based manga retrieval using manga109 dataset," *Multimedia tools and applications*, vol. 76, pp. 21 811–21 838, 2017.
- [29] A. Hore and D. Ziou, "Image quality metrics: Psnr vs. ssim," *Proceedings of the 20th International Conference on Pattern Recognition (ICPR)*, pp. 2366–2369, 2010.
- [30] Z. Wang, A. C. Bovik, H. R. Sheikh, and E. P. Simoncelli, "Image quality assessment: from error visibility to structural similarity," *IEEE Transactions on Image Processing*, vol. 13, no. 4, pp. 600–612, 2004.
- [31] H. Guo, Y. Guo, Y. Zha, Y. Zhang, W. Li, T. Dai *et al.*, "Mambairv2: Attentive state space restoration," *arXiv preprint arXiv:2411.15269*, 2024, online.
- [32] S. Moustafa, "Torch operation counter," Available: <https://github.com/SamirMoustafa/torch-operation-counter>, 2023, online.
- [33] Z. Yang, J. Li, H. Zhang, D. Zhao, B. Wei, and Y. Xu, "Restore-rwkv: Efficient and effective medical image restoration with rwkv," *arXiv preprint arXiv:2407.11087*, 2024, online.
- [34] H. Hou, P. Zeng, F. Ma, and F. R. Yu, "Visualrwkv: Exploring recurrent neural networks for visual language models," *arXiv preprint arXiv:2406.13362*, 2024, online.